Hydroxyapatite/iron oxide nanocomposite prepared by high energy ball milling

Milica Vučinić Vasić[1,*], Bratislav Antić[2], Marko Bošković[2], Aleksandar Antić[1], Jovan Blanuša[2]

[1]Faculty of Technical Sciences, University of Novi Sad, Trg D. Obradovica 6, 21000 Novi Sad, Serbia
[2]Institute of Nuclear Sciences "Vinča", University of Belgrade, P.O. Box 522, 11001 Belgrade, Serbia

Abstract

Nanocomposites (HAp/iron oxide), made of hydroxyapatite (HAp) and ferrimagnetic iron oxide, were synthesized by high-energy ball milling a mixture consisting of iron oxide nanoparticles and the starting materials used for the HAp synthesis: calcium hydrogen phosphate anhydrous ($CaHPO_4$), and calcium hydroxide ($Ca(OH)_2$). Two HAp/iron oxide samples with the magnetic phase content of 12 and 30 wt.% were prepared and their microstructure, morphology and magnetic properties were analysed by X-ray diffraction and transmission electron microscopy. Furthermore, the measurement of particle size distribution was performed by laser scattering, and temperature/field dependence on magnetization was determined. X-ray diffraction data confirmed the formation of two-phased samples (HAp and spinel iron oxide) without the presence of any other parasite phase. The shape of particles was nearly spherical in both samples, ranging from only a few to several tens of nanometres in diameter. These particles formed agglomerates with the most common value of the number-based particle size distribution of 380 and 310 nm for the sample with 12 and 30 wt.% of iron oxide, respectively. Magnetization data showed that both HAp/iron oxide composites had superparamagnetic behaviour at room temperature.

Keywords: nanocomposites, hydoxyapatite, milling, X-ray diffraction (XRD), magnetic measurements

I. Introduction

Over the last fifty years, magnetic nanocomposites, in core-shell or hybrid form, have been intensively investigated due to their unique magnetic properties useful for application in many fields, one of them being medicine [1,2]. For example, magnetic core-shell nanocomposites are excellent candidates for hyperthermia antitumour treatment [3,4]. Nanocomposites for medical application mainly consist of magnetite (Fe_3O_4) or maghemite (γ-Fe_2O_3) because their magnetic moments are high and they are not toxic in small concentrations [5].

Calcium phosphate salts are essential constituents of bones and teeth [6], and therefore, hydroxyapatite ($Ca_{10}(PO_4)_6(OH)_2$), denoted as HAp, is the most stable in body fluid and it is the most similar to the mineral part of bones [9]. Considering their remarkable biocom-

patibility and bioactivity properties, many HAp based materials in the form of powders, granules, composites etc. have been developed in the last few decades [7–9]. Several studies have shown that nano HAp can be used as a drug carrier system [10–12], while modified HAp could be used for the treatment of various types of cancer [13,14].

Nanocomposites made from magnetic material and certain non-magnetic biocompatible component are very important from the technological point of view. These materials include, for instance, coating of magnetic nanoparticles with polymer [15], synthetic silica [16], hydroxyapatite [17], and other different biocompatible materials. Among these, HAp/iron oxide nanocomposites attract great scientific attention. Thus, magnetite/hydroxyapatite composite is a promising material for hyperthermia treatments [18]; increase in magnetite concentrations significantly increases the loading capacity of protein for Fe_3O_4@HAp composites [19];

*Corresponding author: tel: +381214852276,
e-mail: *milicavv@uns.ac.rs*

magnetic hydroxyapatite microspheres possess better drug release property compared to microspheres without ferrite component [20]; HAp doped with iron oxide exhibits better solubility in physiological solution as well as enhanced radiopacity and osteoblast proliferation activity compared to pure HAp [21,22]; yield and tensile strength of iron/hydroxyapatite composites decrease with increasing HAp content [23]; HAp/iron oxide composites are efficient in the removal of heavy metal ions from water [24]; and HAp/ferrite nanocomposites are magnetically recyclable catalysts [25].

A wide range of promising applications of the HAp based nanomaterials has supported the development of numerous methods for their synthesis. The mechanochemical method is a simple way to produce various HAp based nanocomposites [18,26,27]. A typical process requires starting materials with Ca^{2+} and PO_4^{3-} ions that are mixed in an appropriate molar ratio and powdered in a planetary ball mill [18]. Besides the type of reagents, other adjustable processing parameters in the synthesis procedure are: the type of milling medium, the type of atmosphere, composition and diameter of milling balls, duration of the milling process, powder-to-ball mass ratio, the angular velocity of vial and the angular velocity of the platform to which the vial filled with milling material is attached. Nanoparticles with diverse morphology (the most common forms being sphere, rod, tube, prism etc.) and a very high crystallinity degree can be achieved by applying this method [7]. One of the main limitations of the mechanochemical synthesis of magnetic nanocomposites is the possibility of the formation of impurity phases, which depends on the concentration of magnetic ions and could have a negative influence on their magnetic properties [28].

This is the first time that the synthesis of nanocomposites HAp/iron oxide by high-energy ball milling of spinel iron oxide nanoparticles, calcium hydrogen phosphate anhydrous, $(CaHPO_4)$ and calcium hydroxide $(Ca(OH)_2)$ was performed. Samples with target iron oxide composition of 30 wt.% (according to our knowledge, the upper limit of magnetite content into HAp/Fe_3O_4 nanocomposite that is suitable for biomedical applications) and 12 wt.% were prepared. The prepared samples were analysed by different techniques such as X-ray powder diffraction (XRPD), transmission electron microscopy (TEM), light scattering particle-size distribution analysis and magnetic measurements.

II. Experimental

High-energy ball milling (HEBM) was used for the preparation of HAp/iron oxide composites with different amount of HAp and iron oxide. Iron oxide nanoparticles were synthesized using a slightly modified Massart's method [29]. In brief, 1.5 M NaOH was added to the initial solution of $FeSO_4 \cdot 7H_2O$ and $FeCl_3 \cdot 6H_2O$. Molar ratio of $FeSO_4 \cdot 7H_2O$ and $FeCl_3 \cdot 6H_2O$ was

1 : 2 with the aim of obtaining pure magnetite. After reaching pH = 10, the suspension was heated to 80 °C while being vigorously stirred for 30 min. The coprecipitate was then rinsed repeatedly in deionized water until neutral pH was obtained.

Anhydrous calcium hydrogen phosphate $(CaHPO_4$, Merck) and calcium hydroxide $(Ca(OH)_2$, Merck) were used as starting materials to obtain HAp. Formation of HAp can be described using the following equation:

$$6\,CaHPO_4 + 4\,Ca(OH)_2 \longrightarrow Ca_{10}(PO_4)_6(OH)_2 + 6\,H_2O$$
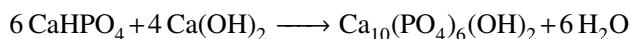
In order to obtain the iron oxide concentration of 30 and 12 wt.% in HAp/iron oxide, 18 mmol of $CaHPO_4$ and 12 mmol of $Ca(OH)_2$ were added into 65 ml and 20 ml of the previously prepared magnetic nanoparticles water suspensions (the iron oxide concentration was 20 mg/ml). The mixtures were stirred vigorously with a magnetic stirrer, after which they were kept in a sterilizer at the temperature of 70 °C for 10 min, resulting in partial water evaporation. Mechanochemical milling was carried out in the Fritsch Pulverisette mill using a tungsten carbide bowl and balls (diameter 20 mm). The charge to the ball ratio and rotational speed were 1 : 20 and 600 rpm, respectively. During the milling, small amounts of samples were taken from the opened balls for XRPD at ten-minute intervals. The final samples, obtained after 130 min of milling, were denoted by SI (composite with targeted 30 wt.% of iron oxide) and SII (composite with targeted 12 wt.% of iron oxide).

The data on X-ray powder diffraction were collected by the Rigaku Smartlab 3 kW X-ray powder diffractometer. The scanning range was 15–115° in 2θ with a step of 0.05° and a scanning speed of 1 °/min.

Transmission electron micrographs were determined by using the JEOL JEM 2100 transmission electron microscope (TEM) operating at 200 kV. The samples were dispersed in acetone, and the obtained suspensions were dropped on lacey carbon film on a 300-mesh copper grid.

The particle size distribution was determined by using the Malvern Mastersizer 2000 particle size analyser capable of analysing particles between 0.01 and 2000 μm. The fluid that was used as a dispersion medium (dispersant) was distilled water. Hydro2000 Micro Precision, the dispersion unit for small amounts of material, was used for the measuring done in the dynamic mode with pump speed of 2500 rpm and ultrasonic regime. The results were recorded as the particle volume-based percentage after which they were recalculated as the particle number-based percentage.

Magnetic properties of the samples were characterized by the magnetization measurement versus applied field $M(H)$ at 300 K as well as by ZFC and FC magnetization from 5 to 300 K in the applied field of 100 Oe. All the measurements were done on the Quantum Design SQUID device MPMS-XL5.

III. Results and discussion

3.1. Composite structure

The formation of HAp/iron oxide composite was monitored by XRPD. Figure 1a shows XRPD patterns of the iron oxide nanoparticles and starting materials for the HAp synthesis. The most intensive diffraction peaks for $Ca(OH)_2$, $CaHPO_4$ and spinel iron oxide were recorded in 2θ range 22–42° (Fig. 1a). Iron oxide peaks were broader than $Ca(OH)_2$ and $CaHPO_4$ due

to a smaller crystallite size in comparison to the starting materials used for the HAp synthesis. Figures 1b and 1c depict XRPD patterns of the SI and SII samples measured after a different milling time. It can be seen that, after 40 min of milling, the peaks of the starting materials were clearly visible at diffractograms of both samples, as well as the additional peaks between 31° and 33°. These peaks indicated the formation of HAp phase. A significant increase in HAp peaks intensity was recorded after 70 min of milling (Figs. 1b and 1c). The diffraction peaks of the starting materials for the HAp synthesis were still visible indicating that the formation of HAp was not completed after 70 min of milling. The most intense diffraction peaks corresponding to $Ca(OH)_2$ and $CaHPO_4$ disappeared after 130 min of milling. XRPD patterns determined for both samples with a longer counting time (Fig. 2) confirmed that the mechanochemical reaction was completed.

XRPD patterns of both samples showed the presence of iron oxide with spinel structure (Fe_3O_4, γ-Fe_2O_3) and HAp phases only. Impurities from vials and balls material are common in mechanochemical synthesis. Combination of relatively low speed, short milling time and hard mill equipment (made of tungsten carbide) resulted in no observable XRD peaks from WC for both investigated samples. Coprecipitation method in this research was performed in order to provide pure magnetite. During the synthesis, milling and storage in ambient atmosphere magnetite nanoparticles could be partly oxidized to maghemite [1,30]. The fact that diffraction peaks indicating the presence of maghemite in space group $P4_132$ were not visible in XRD patterns of both investigated samples cannot provide any definite proof about the exact magnetic phase content. The determination of magnetite/maghemite precise content ratio was not of crucial importance regarding the scope of the synthesized composites (magnetic hyperthermia related to bone tissue) due to minor differences in magnetic behaviour of magnetite and maghemite.

XRD data measurement with a scanning speed of 1 °/min were used for the confirmation of the composite formation, refinement of crystal structure and determination of microstructure parameters (crystallite size). Considering all previously mentioned the two-phase structural model: spinel iron oxide - space group $Fd\bar{3}m$, and HAp - space group $P6_3/m$, was used for the crystal structure refinement in the FullProf computer program. Rietveld refinement results are presented in Fig. 2 for both samples. Structural parameters that were refined for both phases were lattice parameters, overall temperature factors, the scale factor and atomic position coordinates. The attempts to refine the occupation numbers did not provide stable refinements, which is frequently the case with nano-sized crystal domains since the calculation of scattering factors in the Rietveld procedure normally assumes "infinite" and regular periodic structures (i.e. macrocrystals). Table 1 shows determined structural and microstructural parameters of interest.
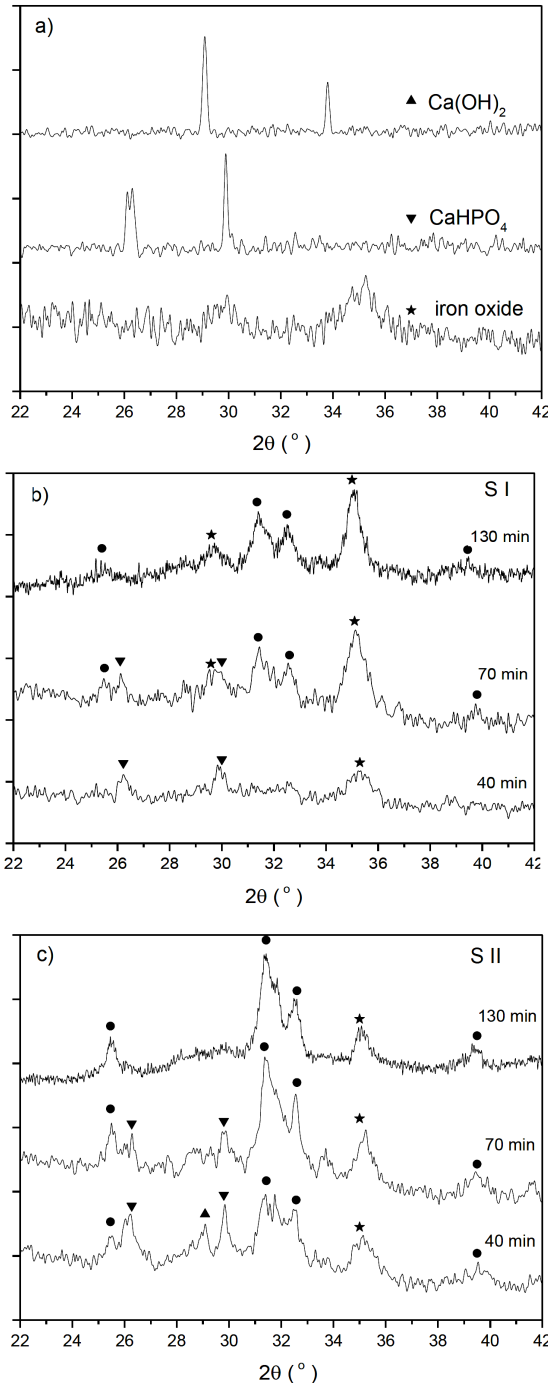

Figure 1. XRD patterns of HAp/iron oxide composites: a) starting materials, b) sample SI and c) sample SII – symbol ● denotes HAp peaks
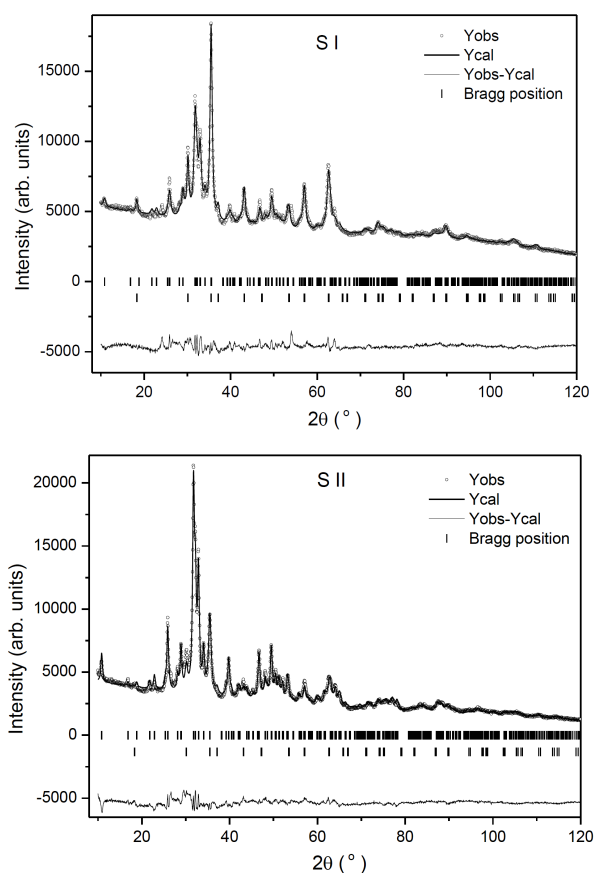
Figure 2. XRD patterns of HAp/iron oxide composites - final Rietveld refinement plot (vertical bars indicate the positions of the crystallographic reflection for HAp (first-row tick marks) and spinel iron oxide (second row) phases)

The results of the quantitative phase analysis obtained from the Rietveld refinement should be taken with careful consideration. Firstly, considering the fact that the Rietveld errors only indicated how well the model fitted the observed diffraction pattern, they did not represent the estimates of the true errors of the sample composition. Secondly, although the quantitative phase analysis using the Rietveld method is capable of yielding accurate results for well crystallized bulk materials, it loses its power for nanocrystalline materials because their diffraction patterns become broad and less defined. In this respect, the obtained composition (in wt.%), given in Table 1, should be interpreted as semi-quantitative and they comply well with the target values (30 wt.% of iron oxide in the sample SI and 12 wt.% in the sample SII).

The lattice parameters for iron oxide and HAp phases in both samples were slightly different from the values reported for bulk magnetite JCPDS Card No. (79-0417) ($a = 8.394$ Å), bulk maghemite JCPDS Card No. 39-1346 ($a = 8.346$ Å) and bulk HAp JCPDS Card No. 74-0565 ($a = 9.424$ Å, $c = 6.879$ Å). The lattice parameters of nanocrystalline materials in general can be significantly different from the bulk or single crystal materials. The lattice parameters of HAp obtained from the mandible bone with the crystallite size of 10 nm were reported to be 9.4184 Å and 6.8837 Å, while for the carbonated HAp synthesized by the chemical precipitation with the crystallite size of 8 nm were 9.3971 Å and 6.9027 Å [31]. Smoleń *et al.* [32] synthesized hydroxyapatite nanopowder with a programmed resorption rate with lattice parameters ranging from 9.423–9.433 Å to 6.8745–6.8777 Å. The lattice parameter of nanocrystalline iron oxide in the investigated samples was found to be slightly smaller than the one for the corresponding bulk magnetite but larger than bulk maghemite materials. This could be caused by possible magnetite particle oxidation during milling resulting in a magnetite core with a surrounding maghemite shell [33,34].

The crystallite size was obtained based on the line profile analysis of the X-ray diffraction data. Isotropic X-ray line broadening was analysed by the refinement of TCH-pV function parameters (isotropic effect). The instrumental broadening was characterized through the instrumental resolution function that had been obtained for the LaB$_6$ standard. The average crystallite size obtained from Rietveld analysis, given in Table 1, was found to be quite similar for both phases of prepared composite samples. The obtained values showed nanocrystalline nature of all phases in the prepared composites.

Typical TEM images of the prepared composite samples are presented in Fig. 3. Iron oxide and HAp nanoparticles could not be distinguished with certainty from TEM images. The samples were investigated at different magnifications. Low magnification TEM images showed that agglomerates were in the micrometer size range for both samples, as it is shown in Fig. 3a for the sample SI. Higher magnification images (Figs. 3b and 3c) showed that agglomerates in both samples were created from much smaller particles that were nearly spherical in shape, whose diameter was between 7–30 nm and 10–40 nm for the sample SI and SII respectively. The crystallite size determined from X-ray line-

Table 1. Structural and microstructural parameters

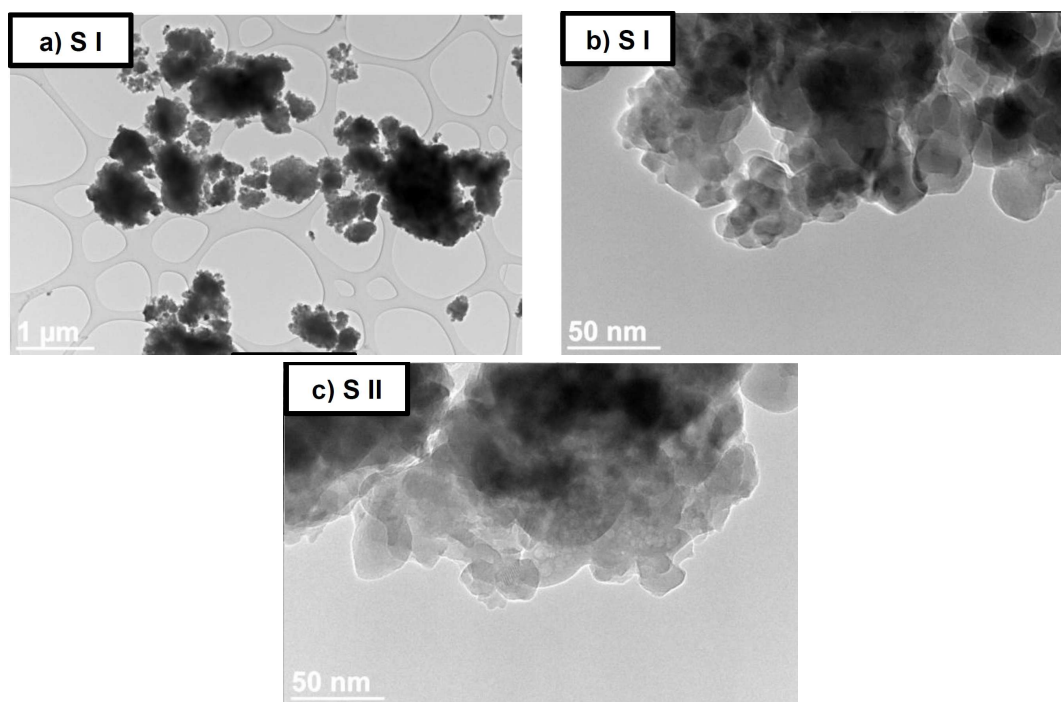| Sample	Phase	Composition [wt.%]	Lattice parameters [Å]	Average crystallite size [nm]
SI	spinel iron oxide	33.9(2)	8.388(1)	15
	HAp	66.0(4)	9.412(1)	9
			6.884(1)	
SII	spinel iron oxide	12.7(4)	8.388(1)	10
	HAp	87(1)	9.431(1)	14
			6.881(1)	

Figure 3. Representative TEM images of HAp/iron oxide composites

broadening analysis was of the same order of magnitude as the size of those primary particles observed by TEM.

The particle-size distribution was analysed by the Mastersizer 2000. The Applied Mie light scattering theory assumes that the particles are spheres and that the results obtained for their size represents equivalent sphere diameters. The recorded number-based particle size distribution (PSD) curves are shown in Fig. 4. PSD results showed that the number of particles smaller than 200 nm was negligible in both samples, as well as that particles greater than 2 μm existed in both samples. Taking into account these results together with the above-mentioned ones from the TEM image analysis and XRPD, it can be concluded that the obtained size distribution curves were obviously related to agglomerates. The key ele-
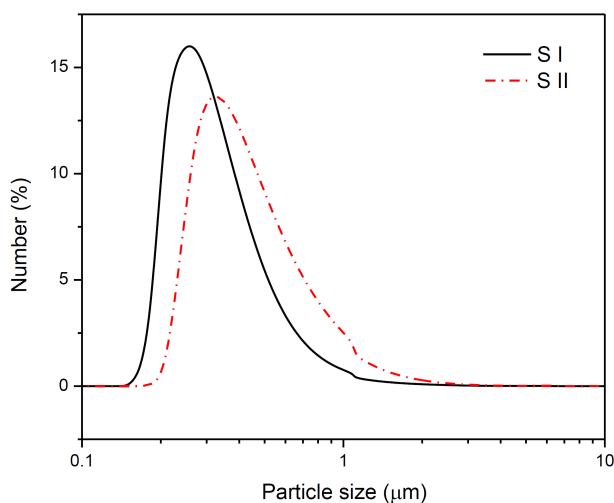
ments influencing the intensity of agglomeration are the synthesis method and the type of material (Van der Walls forces, effective surface area). The greatest influence is on the side of the synthesis method which provides a high degree of agglomeration in general. For the purpose of avoiding the formation or breaking of agglomerates, the samples were treated with ultrasound prior and during the measurements by the Mastersizer 2000, but such de-agglomeration procedure did not result in the breaking of agglomerates. The agglomeration of HAp/Fe_3O_4 was also reported by other authors. For example, agglomerates in the range of 100–350 nm were observed for nanocomposite obtained by wet milling [35]. PSD parameters are given in Table 2. Parameters $d_{0.1}$, $d_{0.5}$ and $d_{0.9}$ indicate particle (agglomerate) diameters below which are 10%, 50% and 90% of the cumulative distribution curve measured on the number basis. The values of the mentioned parameters as well as the most common values of the frequency number-based distribution curves (mode) indicate slightly larger agglomerates in the sample SII. We believe that the different agglomerate size in two samples originates mostly from different balance between constituent materials.

Table 2. Number-based PSD parameters

Sample	$d_{0.1}$ [nm]	$d_{0.5}$ [nm]	$d_{0.9}$ [nm]	Mode [nm]
SI	262	370	689	310
SII	328	496	1067	380

3.2. Magnetic properties

It is a well-known fact that the bulk magnetite and maghemite shows ferrimagnetic behaviour. However, when down-scaled to a single domain particles, the sur-
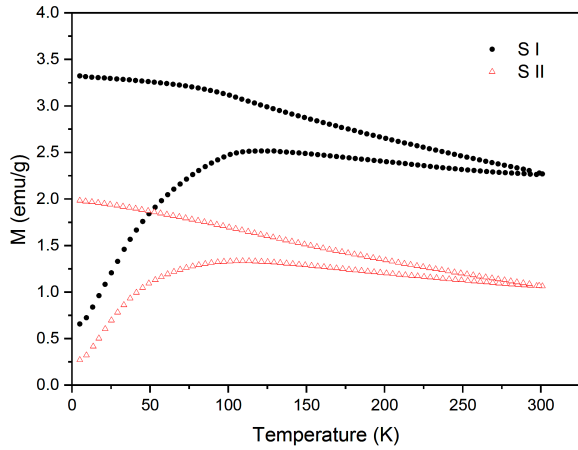

Figure 4. Particle (agglomerate) size distribution curves of HAp/iron oxide composites

Figure 5. Temperature dependence on ZFC and FC magnetization of HAp/iron oxide composites

face disorder effects and decrease in anisotropy energy lead to superparamagnetism, sometimes joined with collective phenomena like spin-glass or exchange bias in core-shell structures, or superspin-glass in the presence of sufficiently strong interparticle interactions [36–38].

Each studied composite sample consisted of one magnetic phase (ferrimagnetic iron oxide) and one non-magnetic phase (HAp). The effects of composition on the basic magnetic properties, saturation magnetization and coercivity were considered. Figure 5 illustrates the temperature dependence on ZFC and FC magnetization in the samples. The maximum temperature in the ZFC curve was 120 K and 110 K for the sample SI and SII, respectively. The maximum in the ZFC magnetization curve was typical for both superparamagnetic and super-spin-glass states, that is, T_{max} was the blocking temperature and freezing temperature, respectively. FC magnetization showed constant increase alongside temperature decrease for both samples. Such behaviour was typical for superparamagnetic systems [39] and indicated the absence or low magnetic interparticle interaction. In addition, the absence of ZFC-FC curves overlaps up to 300 K was a clear indication that some portion of magnetic particles remained blocked at room temperature, thus implying wide particle-size distribution.

Saturation magnetization and coercivity values were influenced by many factors such as: crystallite size, microstrain, presence of parasitic phases, cation distribution, interparticle interaction, etc. The hysteresis loops of the samples, recorded at 300 K, are shown in Fig. 6. Magnetization values were calculated using the total weight of the composite sample (Fig. 6a). In order to evaluate the state of the magnetic phase, the magnetization values were also calculated per gram of iron oxide (Fig. 6b). Data overlap, Fig. 6b, points to the fact that the same particles were used for the synthesis of the composites. Coercivity values (H_C) were found to be 95 and 80 Oe for the SI and SII, respectively. For both samples, magnetization was not saturated up to the maximum applied field of 5 T at 300 K, which is com-

monly attributed to the disordered layer at the surface of the nanoparticles. This effect becomes more prominent with a decreasing particle-size [40].

The values for the average magnetic particle size and magnetization saturation (M_S) at 300 K were obtained based on the weighed Langevin fit. A log-normal particle-size distribution:

$$g(D) = \frac{1}{\sqrt{2\pi} \cdot \sigma \cdot d} \exp\left(-\frac{\ln\left(\frac{D}{D_0}\right)^2}{2\sigma^2}\right) \qquad (1)$$

was used as a weighing factor. In the equation, D_0 and σ are distribution parameters, and D is the particle diameter. The complete fitting function form is:

$$M(B) = M_S \int g(D) \cdot L(D, B, T)\, dD + \chi B \qquad (2)$$

where $L(D, B, T)$ is the Langevin function in which the particle moment is represented by a product of magnetization saturation and particle volume. D, B and T are the particle diameter, magnetic field induction and temperature, respectively. The χB represents an additional linear term originating from the nanoparticle disordered surface layer and HAp phase. During the fitting procedure, free parameters were magnetization saturation M_S, dis-
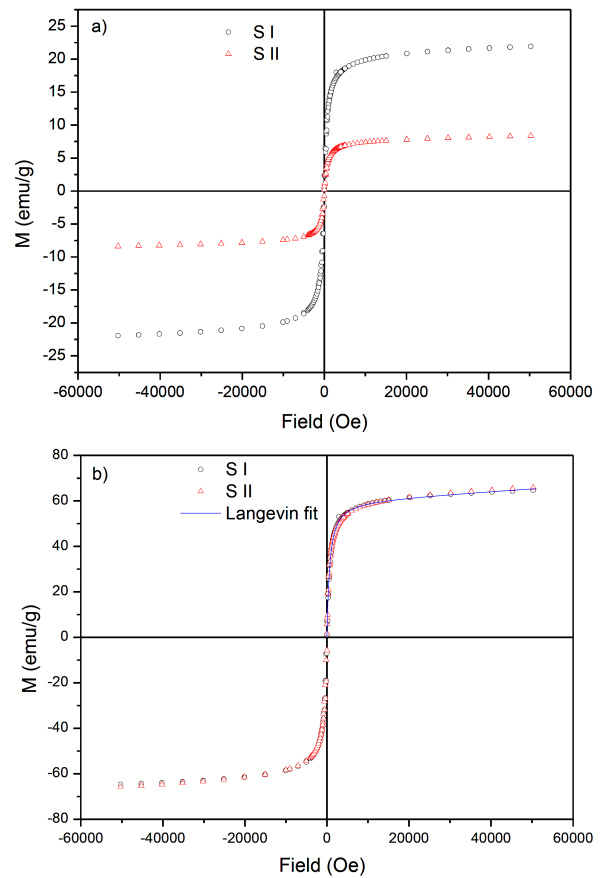

Figure 6. Hysteresis loops of HAp/iron oxide composites recorded at 300 K, calculated per gram of: a) the sample and b) magnetic phase (line represents the best fit)

tribution parameters d_0 and σ, and linear parameter χ. Both hysteresis loops were used simultaneously for the fitting. As a result, the acquired value for magnetization saturation was $M_S = 60$ emu/g, and the average diameter calculated from the distribution parameters was $d_{avg} = 9$ nm with a standard deviation of 3 nm. The acquired size complies well with the values obtained from the Rietveld refinement and the TEM analysis.

Saturation magnetization of the bulk Fe_3O_4 and γ-Fe_2O_3 were 92–100 emu/g and 60–80 emu/g, respectively [30]. The reduction in saturation magnetization in comparison to the values of the bulk can normally be observed for nanomaterials due to the presence of magnetically disordered surface. However, it also strongly depends on the relative volume ratio between ordered and disordered regions within the particle. For example, Sneha and Sundaram [35] reported the saturation magnetization of only 7.34 emu/g at 300 K in iron oxide-hydroxyapatite nanocomposite prepared by the wet milling of Fe_3O_4 and HAp (0.70 w/w, respectively), with the average particle-size of Fe_3O_4 in the range of 50–70 nm. That value of saturation magnetization was lower than reported one, in spite of the fact that both of our samples were composed of smaller particles, which indicated higher crystallinity of the samples examined in this study.

IV. Conclusions

High-energy ball milling of the mixture of iron oxide nanoparticles, anhydrous calcium hydrogen phosphate and calcium hydroxide was successfully applied for the first time to synthesize HAp/iron oxide composites with 30 wt.% of iron oxide (SI) and 12 wt.% of iron oxide (SII). The crystallite size obtained by the line profile analysis of the X-ray diffraction data was of the same order of magnitude as the particle size obtained from the TEM images according to which the particle size ranged from 7 to 30 nm for the sample SI and from 10 to 40 nm for the sample SII. These nanoparticles formed agglomerates in distilled water suspension. 90% of these agglomerates were smaller or equal to ≈ 700 nm and ≈ 1000 nm for the samples SI and SII, respectively. The small particle-size resulted in the insignificant reduction in magnetization compared to the bulk material, as well as in the absence of its complete saturation up to the field of 5 T. Both of the mentioned effects caused strength lowering of interparticle magnetic interaction and blocked behaviour of iron oxide (or even super spin glass state) below ≈ 120 K for the sample SI and ≈ 110 K for the sample SII. This type of material would be an appropriate candidate for biomedical applications such as magnetic hyperthermia and carrier for medicaments, but not in this state of agglomeration.

References

1. A. Inukai, N. Sakamoto, H. Aono, O. Sakurai, K. Shinozaki, H. Suzuki, N. Wakiya, "Synthesis and hyperthermia property of hydroxyapatite-ferrite hybrid particles by ultrasonic spray pyrolysis", *J. Magn. Magn. Mater.*, **323** [7] (2011) 965–969.

2. R. Karunamoorthi, G. Suresh Kumar, A. Ishwar Prasad, R. Kumar Vatsa, A. Thamizhavel, E. Girija Kreedapathy, "Fabrication of a novel biocompatible magnetic biomaterial with hyperthermia potential", *J. Am. Ceram. Soc.*, **97** [4] (2014) 1115–1122.

3. G. Zhang, Y. Liao, I. Baker, "Surface engineering of core/shell iron/iron oxide nanoparticles from microemulsions for hyperthermia", *Mater. Sci. Eng. C*, **30** [1] (2010) 92–97.

4. S.H. Liao, C.H. Liu, B.P. Bastakoti, N. Suzuki, Y. Chang, Y. Yamauchi, F.H. Lin, K. Wu, "Functionalized magnetic iron oxide/alginate core-shell nanoparticles for targeting hyperthermia", *Int. J. Nanomedicine*, **10** (2015) 3315–3328.

5. W.N. Erber, "Red blood cell disorders", pp. 496–508 in *Clinical Pharmacology*. Eds. by P.N. Bennett, M.J. Brown, P. Sharma, Elsevier-Churchill Livingstone, London 2012.

6. P. Malmberg, H. Nygren, "Methods for the analysis of the composition of bone tissue, with a focus on imaging mass spectrometry (TOF-SIMS)", *Proteomics*, **8** [18] (2008) 3755–3762.

7. M. Sadat-Shojai, M.T. Khorasani, E. Dinpanah-Khoshdargi, A. Jamshidi, "Synthesis methods for nanosized hydroxyapatite with diverse structures", *Acta Biomater.*, **9** [8] (2013) 7591–7621.

8. S. Khoshsima, A.Z. Alshemary, A. Tezcaner, S. Surdem, Z. Evis, "Impact of B_2O_3 and La_2O_3 addition on structural, mechanical and biological properties of hydroxyapatite", *Process. Appl. Ceram.*, **12** [2] (2018) 143–152.

9. M.P. Ferraz, F.J. Monteiro, C.M. Manuel, "Hydroxyapatite nanoparticles: A review of preparation methodologies", *J. Appl. Biomater. Func. Mater.*, **2** [2] (2004) 74–80.

10. Y. Han, X. Wang, S. Li, "A simple route to prepare stable hydroxyapatite nanoparticles suspension", *J. Nanopart. Res.*, **11** [5] (2009) 1235–1240.

11. M.P. Ferraz, A.Y. Mateus, J.C. Sousa, F.J. Monteiro, "Nanohydroxyapatite microspheres as delivery system for antibiotics: release kinetics, antimicrobial activity, and interaction with osteoblasts", *J. Biomed. Mater. Res. A*, **81** (2007) 994–1004.

12. S.S. Syamchand, G. Sony, "Multifunctional hydroxyapatite nanoparticles for drug delivery and multimodal molecular imaging", *Microchim. Acta*, **182** [9/10] (2015) 1567–1589.

13. C.H. Hou, S.M. Hou, Y.S. Hsueh, J. Lin, H.C. Wu, F.H. Lin, "The in vivo performance of biomagnetic hydroxyapatite nanoparticles in cancer hyperthermia therapy", *Biomaterials*, **30** [23-24] (2009) 3956–3960.

14. J. Li ,Y. Yin, F. Yao, L. Zhan, K. Yao, "Effect of nano- and micro-hydroxyapatite/chitosan-gelatin network film on human gastric cancer cells", *Mater. Lett.*, **62** [17-18] (2008) 3220–3223.

15. N. Nitin, L. La Conte, O. Zurkiya, X. Hu, G. Bao, "Functionalization and peptide-based delivery of magnetic nanoparticles as an intracellular MRI contrast agent", *J. Biol. Inorg. Chem.*, **9** [6] (2004) 706–712.

16. H.H. P. Yiu, P.A. Wright, N.P. Botting, "Enzyme immobilisation using SBA-15 mesoporous molecular sieves with functionalised surfaces", *J. Mol. Catal. B Enzym.*, **15** [1-3] (2001) 81–92.

17. S. Mondal, P. Manivasagan, S. Bharathiraja, S.S.M. Madhappan, V. Nguyen, H.H. Kim, S.Y. Nam, D.L. Kang, J. Oh, "Hydroxyapatite coated iron oxide nanoparticles: A promising nanomaterial for magnetic hyperthermia cancer treatment", *Nanomaterials*, **7** [11] (2017) 426.

18. T. Iwasaki, R. Nakatsuka, K. Murase, H. Takata, H. Nakamura, S. Watano, "Simple and rapid synthesis of magnetite/hydroxyapatite composites for hyperthermia treatments via a mechanochemical route", *Int. J. Mol. Sci.*, **14** [5] (2013) 9365–9378.

19. G. Bharath, D. Prabhu, D. Mangalaraj, C. Viswanathana, N. Ponpandian, "Facile in situ growth of Fe_3O_4 nanoparticles on hydroxyapatite nanorods for pH dependent adsorption and controlled release of proteins", *RSC Adv.*, **4** [94] (2014) 50510–50520.

20. Y.P. Guo, L. H. Guo,Y. Yao, C.Q. Ning, Y.J. Guo, "Magnetic mesoporous carbonated hydroxyapatite microspheres with hierarchical nanostructure for drug delivery systems", *Chem. Commun.*, **47** [44] (2011) 12215–12217.

21. O. Kuda, N. Pinchuk, L. Ivanchenko, O. Parkhomey, O. Sych, M. Leonowicz, R. Wroblewski, E. Sowka, "Effect of Fe_3O_4, Fe and Cu doping on magnetic properties and behaviour in physiological solution of biological hydroxyapatite/glass composites", *J. Mater. Process. Technol.*, **209** [4] (2009) 1960–1964.

22. M. Ajeesh, B.F. Francis, J. Annie, P.R.H. Varma, "Nano iron oxide-hydroxyapatite composite ceramics with enhanced radiopacity", *J. Mater. Sci. Mater. Med.*, **21** [5] (2010) 1427–1434.

23. M. Dehestani, E. Adolfsson, L.A. Stanciu, "Mechanical properties and corrosion behavior of powder metallurgy iron-hydroxyapatite composites for biodegradable implant applications", *Mater. Des.*, **109** (2016) 556–569.

24. M. Elkady, H. Shokry, H. Hamad, "Microwave-assisted synthesis of magnetic hydroxyapatite for removal of heavy metals from groundwater", *Chem. Eng. Technol.*, **41** [3] (2018) 553–562.

25. M. Azaroon, A.R. Kiasat, "Silver nanoparticles engineered β-cyclodextrin/γ-Fe_2O_3@hydroxyapatite composite: Efficient, green and magnetically retrievable nanocatalyst for the aqueous reduction of nitroarenes", *Catal. Lett.*, **148** [2] (2018) 745–756.

26. C.C. Silva, A.G. Pinheiro, R.S. de Oliveira, J.C. Goes, N. Aranha, L.R.de Oliveira, A.S.B. Sombra, "Properties and in vivo investigation of nanocrystalline hydroxyapatite obtained by mechanical alloying", *Mater. Sci. Eng. C*, **24** [4] (2004) 549–554.

27. M.H. Fathi, E. Mohammadi Zahrani, "Mechanical alloy-ing synthesis and bioactivity evaluation of nanocrystalline fluoridated hydroxyapatite", *J. Cryst. Growth*, **311** [5] (2009) 1392–1403.

28. W. Pon-On, S. Meejoo, I.M. Tang, "Substitution of manganese and iron into hydroxyapatite: Core/shell nanoparticles", *Mater. Res. Bull.*, **43** [8-9] (2008) 2137–2144.

29. R. Massart, "Preparation of aqueous magnetic liquids in alkaline and acidic media", *IEEE Trans. Magn.*, **17** [2] (1981) 1247–1248.

30. R.M. Cornell, U. Schwertmann, *The Iron Oxides: Structure, Properties, Reactions, Occurrences and Uses*, Wiley-VCH, Weinheim 2003.

31. S. Marković, Lj. Veselinović, M. Lukić, Lj. Karanović, I. Bračko, N. Ignjatović, D. Uskoković, "Synthetical bone-like and biological hydroxyapatites: a comparative study of crystal structure and morphology", *Biomed. Mater.*, **6** [4] (2011) 045005.

32. D. Smoleń, T. Chudoba, S. Gierlotka, A. Kedzierska, W. Łojkowski, K. Sobczak, W. Święszkowski, K.J. Kurzydłowski, "Hydroxyapatite nanopowder synthesis with a programmed resorption rate", *J. Nanomater.*, **2012** (2012) 841971.

33. R. Fan, X.H. Chen, Z. Gui, L. Liu, Z.Y. Chen, "A new simple hydrothermal preparation of nanocrystalline magnetite Fe_3O_4", *Mater. Res. Bull.*, **36** [3-4] (2001) 497–502.

34. R. Frison, G. Cernuto, A. Cervellino, O. Zaharko, G.M. Colonna, A. Guagliardi, N. Masciocchi, "Magnetite-maghemite nanoparticles in the 5–15 nm range: Correlating the core-shell composition and the surface structure to the magnetic properties. A total scattering study", *Chem. Mater.*, **25** [23] (2013) 4820–4827.

35. M. Sneha, N.M. Sundaram, "Preparation and characterization of an iron oxide-hydroxyapatite nanocomposite for potential bone cancer therapy", *Int. J. Nanomedicine*, **10** (2015) 99–106.

36. A.G. Kolhatkar, A.C. Jamison, D. Litvinov, R.C. Willson, T.R. Lee, "Tuning the magnetic properties of nanoparticles", *Int. J. Mol. Sci.*, **14** [8] (2013) 15977–16009.

37. M. Van de Voorde, C. Fermon, *Nanomagnetism: Applications and Perspectives*, Wiley-VCH, Weinheim 2017.

38. K. Sarkar, S. Mukherjee, S. Mukherjee, "Structural, electrical and magnetic behaviour of undoped and nickel doped nanocrystalline bismuth ferrite by solution combustion route", *Process. Appl. Ceram.*, **9** [1] (2015) 53–60.

39. M. Perović, A. Marković, V. Kusigerski, J. Blanuša, V. Spasojević, "Spin-glass dynamics in interacting nanoparticle system $La_{0.7}Ca_{0.3}MnO_3$ obtained by mechanochemical milling", *J. Nanopart. Res.*, **13** [12] (2011) 6805–6811.

40. Q. Li, C. W. Kartikowati, S. Horie, T. Ogi, T. Iwaki, K. Okuyama, "Correlation between particle size/domain structure and magnetic properties of highly crystalline Fe_3O_4 nanoparticles", *Sci. Rep.*, **7** (2017) 9894.